

Characterising uniform star formation efficiencies with marginally-stable galactic disks

O. Ivy Wong,^{1,2} G.R. Meurer,^{1,3} Z. Zheng,⁴ T.M. Heckman,⁵ D.A. Thilker⁵
& M.A. Zwaan⁶

¹International Centre for Radio Astronomy Research, ICRAR M468, 35 Stirling Highway, Crawley, WA 6009, Australia

²ARC Centre of Excellence for All-Sky Astrophysics (CAASTRO)

³School of Physics, University of Western Australia, 35 Stirling Highway, Crawley, WA 6009, Australia

⁴National Astronomical Observatories, Chinese Academy of Sciences, 20A Datun Rd, Beijing 100012, China

⁵Department of Physics and Astronomy, Johns Hopkins University, 3701 San Martin Drive, Baltimore, MD 21218, USA

⁶European Southern Observatory, Karl-Schwarzschild-Strasse 2, D-85748 Garching bei M^unchen, Germany

Released 2016 Xxxxx XX

ABSTRACT

We examine the HI-based star formation efficiency (SFE_{HI}), the ratio of star formation rate to the atomic Hydrogen (HI) mass, in the context of a constant stability star-forming disk model. Our observations of HI-selected galaxies show SFE_{HI} to be fairly constant ($\log SFE_{\text{HI}} = -9.65 \text{ yr}^{-1}$ with a dispersion of 0.3 dex) across ~ 5 orders of magnitude in stellar masses. We present a model to account for this result, whose main principle is that the gas within galaxies forms a uniform stability disk and that stars form within the molecular gas in this disk. We test two versions of the model differing in the prescription that determines the molecular gas fraction, based on either the hydrostatic pressure, or the stellar surface density of the disk. For high-mass galaxies such as the Milky Way, we find that either prescription predicts SFE_{HI} similar to the observations. However, the hydrostatic pressure prescription is a more accurate SFE_{HI} predictor for low-mass galaxies. Our model is the first model that links the uniform SFE_{HI} observed in galaxies at low redshifts to star-forming disks with constant marginal stability. While the rotational amplitude V_{max} is the primary driver of disk structure in our model, we find the specific angular momentum of the galaxy may play a role in explaining a weak correlation between SFE_{HI} and effective surface brightness of the disk.

Key words: galaxies: evolution galaxies: formation galaxies: spiral galaxies: ISM galaxies: structure galaxies: dwarf

1 INTRODUCTION

While star formation is largely understood to be a process local to within individual galaxies, the strong correlation between the observed integrated star formation rates (SFR) and total stellar masses (M_*) at both low- and high-redshifts have led astronomers to assume that this is due to a fundamental universal star formation efficiency (SFE), defined as the star formation rate normalised by the gas mass (e.g. Brinchmann et al. 2004; Salim et al. 2007; Schiminovich et al. 2010; Karim et al. 2011; Whitaker et al. 2012; Sobral et al. 2014; Hunt et al. 2015; Popping et al. 2015).

Sub-kiloparsec scale studies of nearby galaxies have found the SFE to be constant when the SFE is measured in terms of the molecular H_2 gas mass (e.g. Leroy et al. 2008). While this is true for the H_2 -normalised SFE_{H_2} , a similar study by Bigiel et al. (2008) found the relationship between the total gas density (sum of both molecular and atomic gas) and the SFR density to show large variation within and between different spiral galaxies. Bigiel et al.

(2008) attribute this variation to the variation of the H_2/HI ratio (R_{mol}) as a function of local environmental factors. Recent observations of massive galaxies (stellar mass, $M_* > 10^{10} M_\odot$) indicate a near constant integrated HI-based SFE (SFE_{HI}) averaging $10^{-9.5} \text{ year}^{-1}$ (Schiminovich et al. 2010; Hunt et al. 2015). Similarly, Huang et al. (2012) found a weakly positive correlation between the SFE_{HI} and the stellar mass of galaxies for an HI-selected sample of galaxies (which typically consists of galaxies less massive than $10^{10} M_\odot$). This is rather surprising since the H_2/HI varies strongly within galaxies and from galaxy to galaxy (Tacconi & Young 1986; Wong & Blitz 2002; Blitz & Rosolowsky 2006; Bigiel et al. 2008; Leroy et al. 2008). *Why is the observed global SFE_{HI} so uniform across all star-forming galaxies?*

In this paper, we construct a model of a galactic disk with a uniform disk stability (Toomre 1964; Zheng et al. 2013) and compare the predicted SFE_{HI} to those observed in nearby galaxies from the the Survey for Ionization in Neutral Gas Galaxies (SINGG; Meurer et al. 2006) and the Survey of Ultraviolet emis-

sion in Neutral Gas Galaxies (SUNGG; Wong 2007). We find that the observed uniformity in global SFE_{HI} across 5 magnitudes of stellar masses can be reproduced by our constant- Q disk model. This is the third paper in a series in which we develop the uniform disk stability model to first account for the gas distribution beyond the optical disk (Meurer et al. 2013), and then the gas and star formation distribution within the optical disk (Zheng et al. 2013). Here we model an integrated property, SFE_{HI} , that connects the inner and outer disk and use a much larger comparison sample than our previous studies.

Section 2 describes the methods used to construct our stable galactic disk models. Section 3 presents the sample of nearby star-forming galaxies used as a comparison to our model star-forming disks. Section 4 discusses the results of our models and compares the model results to those measured from observations of nearby star-forming galaxies. We present our conclusions in Section 5.

2 MODELLING THE STAR FORMATION EFFICIENCY WITH CONSTANT Q DISKS

Here we explore whether the observed behaviour of SFE_{HI} can be explained by a model based on the hypothesis that galaxy disks evolve toward a state of constant disk stability parameter Q (Toomre 1964). Recently, Meurer et al. (2013) showed that hypothesis can explain how HI traces dark matter in the outer parts of galaxies (the so called ‘‘Bosma relation’’; Bosma 1981) by using a single-fluid Q model. On the other hand, Zheng et al. (2013) showed that by assuming a two-fluid (stars and gas) version of the stability parameter Q_{sg} is constant and adopting reasonable assumptions about the Star Formation Law (SFL) we can account for the distribution of the different gas phases and the star formation in nearby galaxies. Both Meurer et al. (2013) and Zheng et al. (2013) dealt with the radial properties of small representative samples of disk galaxies. Here we adapt these models and apply them to a much larger sample of galaxies in order to understand integrated properties, in particular the star formation efficiency, along the full range of star forming galaxies.

2.1 Model overview

In this paper, we use a modified version of the constant two-fluid Q_{sg} model (Zheng et al. 2013) and compare these model results to a different low-redshift sample of galaxies which samples a larger range and variety of star-forming galaxies. Following the results of Zheng et al. (2013), we assume that the gas and stars are both in cold disks; and adopt a constant $Q_{\text{sg}}=1.6$ and fix the gas velocity dispersion (σ_g) at 11 km s^{-1} , following the results of the THINGS survey where the gas velocity dispersion is derived from the 2nd order HI moment maps (Leroy et al. 2008; Zheng et al. 2013). We adopt a Universal Rotation Curve (Persic et al. 1996; Battaner & Florido 2000) to specify the galaxy dynamics and adopt observationally-based scaling relations to specify the stellar mass distribution. We are then in a position to calculate the cold gas distribution, and after separating the gas into molecular and atomic phases, we then calculate the SFR distribution. Here, we consider only the most successful two prescriptions from Zheng et al. (2013) for apportioning the gas into the atomic and molecular phases.

To be more specific, each model galaxy is parameterised as a function of the rotation curve amplitude, V_{max} . As such, we describe the properties of our model galaxies as one-dimensional radial profiles. The stellar mass distribution in our models are deter-

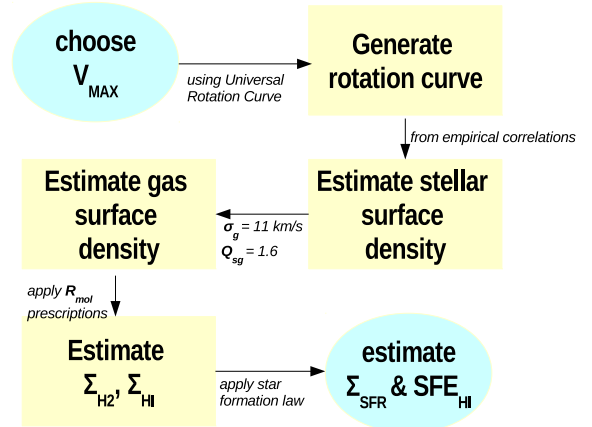


Figure 1. Flow diagram summarising our method for determining SFE_{HI} in our model.

mined via two empirically observed relationships from our sample, namely the Tully-Fisher relationship and the relationship between the stellar surface brightness and V_{max} . We then solve for the gas distribution (Σ_g) using the two-fluid Q approximation described by Wang & Silk (1994). From the resulting Σ_g , we apportion the gas into its molecular and atomic components using two different prescriptions for the molecular to atomic gas ratio (R_{mol}) via: 1) the stellar surface density; and 2) the hydrostatic pressure. Subsequently, we estimate the SFR from the molecular gas content by assuming a largely linear relationship between H_2 and the SFR. Figure 1 shows a flow diagram that summarises how our model determines the SFE_{HI} from our model. More details of our model is described in Section 2.2.

In summary our model is essentially a prescription for how to distribute the gas phases and star formation within galaxies. The essential principle of the model is that galaxy disks evolve to have a uniform stability parameter. In order to calculate the model, the rotation curve of the galaxy and distribution of existing stars is required. There are many important details that this model does not address, such as the mechanism by which the stability parameter is maintained. Presumably it involves feedback between the energy input from supernovae and stellar winds from recent star formation. Recent models by Lehnert et al. (2013) argue that star formation-driven turbulence drives the observed velocity dispersions and that the disk instability is a result of such turbulence. However, how the gas reservoir responds to maintain Q , and the exact value of Q that results are not explicitly addressed. Similarly we use known scaling relations to determine the stellar distribution. But we do not address the underlying physics of these relations. In section 5.1, we show that the model results remain within the scatter of the observations when adjusting the relevant free parameters of the model within known constraints.

2.2 Model details

We employ the Wang & Silk (1994) approximation to specify the two fluid stability parameter Q_{sg} :

$$\frac{1}{Q_{\text{sg}}} = \frac{1}{Q_s} + \frac{1}{Q_g} \quad (1)$$

where Q_s and Q_g are the Toomre stability parameters considering only the stars and gas respectively. For the stars we have

$$Q_s = \frac{\kappa\sigma_{*,r}}{\pi\Sigma_s}, \quad (2)$$

where κ is the epicyclic frequency, $\sigma_{*,r}$ is the velocity dispersion of the stars in the radial direction (in a cylindrical coordinate system), and Σ_s represents the projected surface mass density of stars. Similarly for the gas we have

$$Q_g = \frac{\kappa\sigma_g}{\pi\Sigma_g}, \quad (3)$$

where σ_g is the one-dimensional velocity dispersion of the gas and Σ_g the surface mass density of gas.

We model the SFE_{HI} relation as a one-dimensional sequence as a function of rotation curve amplitude V_{max} . This is used as the driving parameter since it typically is used as shorthand for the halo mass in a standard (Λ) Cold Dark Matter cosmology (e.g. Navarro et al. 1997). We specify the rotation curve shape $V_c(R)$ using the ‘‘Universal Rotation Curve’’ (URC) algorithm of Persic et al. (1996), as implemented by Battaner & Florido (2000). This family of rotation curves is based on long-slit observations of disk galaxies which range in v_{max} from 60–280 km s⁻¹ (Mathewson et al. 1992). The stellar distribution in each galaxy is assumed to be a pure exponential disk (e.g. Freeman 1970); the total stellar luminosity for given V_{max} is given by the Tully-Fisher relationship (TFR; Fisher & Tully 1981; Meyer et al. 2008) while the central surface brightness, and thus scale length are given by the surface brightness – V_{max} relationship, which is a variant of the well-known surface brightness – luminosity relationship (e.g. Disney & Phillipps 1985; Kauffmann et al. 2003). These two relationships are defined in the R -band using SINGG data, and so are well-calibrated to our sample. We note that our model does not take into consideration the contribution from a bulge component. Further discussion on the implications of our ‘‘bulge-less’’ model can be found in Section 5.

In order to convert luminosity to stellar mass we multiply by the mass to light ratio M_*/L_R , noting that $M_R = 4.61^1$ is the absolute magnitude of the Sun in the R -band. Star-forming and passively evolving galaxies are easily distinguished in the optical colour-magnitude space forming the ‘blue cloud’ and the ‘red sequence’ (e.g. Blanton et al. 2003; Bell et al. 2003; Driver et al. 2006). There is a distinct tilt to the ‘blue cloud’ in most optical and ultraviolet colours with the most luminous galaxies being noticeably redder than the dwarfs. Almost all SINGG and SUNGG galaxies reside in the ‘blue cloud’. However we do not have optical photometry for most galaxies except in the R -band. So we use typical SUNGG galaxies with published optical $B - R$ photometry from the NASA/IPAC Extragalactic Database (NED)² at the luminosity extremes of the blue sequence to derive our adopted relationship between M_*/L_R and absolute magnitude M_R

$$\log(M_*/L_R) = -1.578 - 0.0856M_R \quad (4)$$

where M_R is in AB magnitude and the resultant M_*/L_R is in solar units. This relationship was derived from the Bell et al. (2003) stellar population models which assume a ‘‘diet Salpeter’’ IMF.

Figure 2 shows the SINGG based TFR. The sample of galaxies used is single galaxies that have axial ratios $1.6 < a/b < 6$.

¹ All magnitudes are expressed in the ABmag system in this work.

² The NASA/IPAC Extragalactic Database (NED) is operated by the Jet Propulsion Laboratory, California Institute of Technology, under contract with the National Aeronautics and Space Administration.

Total luminosities were measured in an aperture large enough to contain all the R -band light in the SINGG images. Luminosities are corrected for foreground and internal dust absorption using the algorithms in Meurer et al. (2006), which also compiles the adopted distances. The V_{max} values are derived from HI line widths at 50% peak intensity from the HIPASS survey (Meyer et al. 2004; Koribalski et al. 2004) as compiled by Meurer et al. (2006). We follow Meyer et al. (2008) in correcting the line widths for relativity, instrumental resolution, turbulence, and inclination which we derive following the prescription of Meurer et al. (2006). We make an ordinary least squares fit of absolute R band magnitude M_R as a function of $\log(V_{\text{max}})$ to yield our adopted TFR:

$$M_R = -3.90 - 7.622 \log(V_{\text{max}}). \quad (5)$$

The adopted fit is shown as the solid line in Figure 2, while the dashed lines are offset by $\pm 3\sigma$ where $\sigma = 0.95$ mag is the scatter about the fit. Points outside of $\pm 3\sigma$ from the fit are iteratively clipped in our fitting procedure.

This paper is not focussed on the TFR; the measurements are not ‘‘tuned’’ to provide the tightest most accurate relationship. Nevertheless, the TFR we find is of reasonable quality and reaches well in to the dwarf galaxy regime. Several modern studies have shown a break in the TFR for low mass galaxies. McGaugh et al. (2000) and McGaugh (2005) note that the TFR changes slope and has larger scatter for stellar mass $M_* \lesssim 10^9 M_\odot$. They find a tighter more continuous relationship between the baryonic mass (stellar plus gas mass) and the rotational amplitude which they coined the baryonic Tully Fisher Relationship. Recently Simons et al. (2015) and Cortese et al. (2014) found that for $M_* \lesssim 10^{9.5} M_\odot$ there are more extreme outliers to the TFR than at higher masses; and that using the kinematic quantity $S_{0.5}$ which combines contributions from rotation and turbulence restores a tighter relationship. We find an increased scatter about our TFR for dwarf galaxies. For $V_{\text{max}} \leq 96$ km s⁻¹ (corresponding to $M_R > -19.02$ ABmag, and $M_* < 10^{9.5} M_\odot$ following eqs. 5 and 4) the residuals have a dispersion of 1.25 mag, while the dispersion for the points with $V_{\text{max}} > 96$ km s⁻¹ is 0.72 mag (no clipping was done). There is no perceptible change in slope in the TFR for dwarfs within the scatter of our measurements. Meyer et al. (2008) attribute the increased scatter in the TFR of HIPASS galaxies (our parent sample) to the difficulty of estimating the inclination of dwarfs. We likely avoid the extreme outliers found by Simons et al. (2015) because we are using an HI selected sample, pruned of strongly interacting galaxies, with kinematics based on HI line widths. Like their $S_{0.5}$ parameter these widths are determined by contributions from rotation and turbulence; additionally they sample the dynamics to larger radii where the rotation curve is flatter than the ionized gas tracers used by Simons et al. (2015) and Cortese et al. (2014). We conclude that our adopted TFR is adequate for our purposes.

Figure 3 shows the R -band Σ_R versus V_{max} relationship for SINGG galaxies. Here Σ_R is the effective surface brightness - that is the average face-on surface brightness within an aperture containing half of the R -band luminosity. Employing an ordinary least squares fit to these data yields

$$\log(\Sigma_R) = 8.14 + 1.176 \log(V_{\text{max}}). \quad (6)$$

The adopted fit is shown as the solid line, while the dashed lines are offset by $\pm 2\sigma$ where $\sigma = 0.37$ dex is the scatter about the fit. There are no points outside of $\pm 2\sigma$ from the fit. The right axis gives the approximate scaling to stellar mass density Σ_* , as derived by combining eqs. 4, 5 and 6. With the assumption that to first order the surface brightness distribution is a single exponential disk

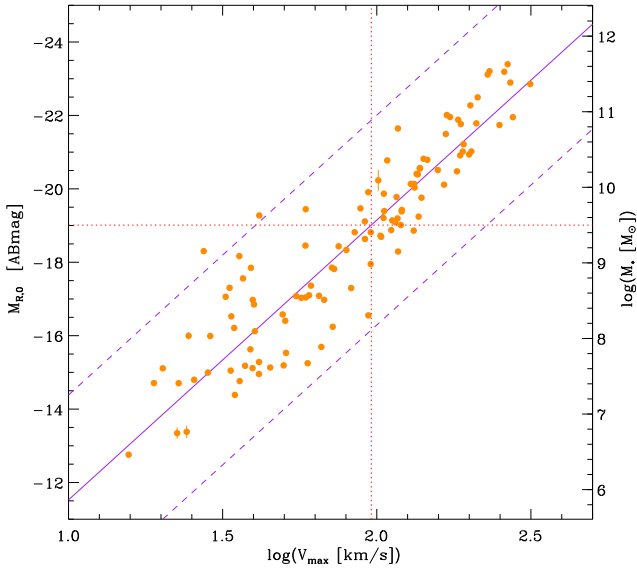


Figure 2. The Tully-Fisher Relationship for SINGG galaxies in the R band, showing the dust corrected absolute R -band magnitude $M_{R,0}$ derived from the SINGG images versus the rotation velocity amplitude V_{\max} derived from HI line widths from the HIPASS survey. Selection criteria for inclusion in this plot and references to the corrections employed are given in the text. An ordinary least squares fit to the data, with iterative clipping of outliers is shown as the solid line. The dashed lines show the $\pm 3\sigma_R$ clipping limit to the fit, where σ_R is the dispersion about the fit. The right axis converts $M_{R,0}$ to stellar mass using eq. 4. The horizontal dotted line shows the stellar mass below which [Simons et al. \(2015\)](#) find the TFR breaks down. The vertical dotted line marks where this intercepts our adopted TFR.

([Freeman 1970](#)) and the standard relationships between effective surface brightness and extrapolated central surface brightness, then the disk scale length is given by

$$R_d = \sqrt{\frac{10^{-0.4(M_R - 4.61)}}{5.647\pi\Sigma_r}}. \quad (7)$$

We follow the prescription given in equation B3 of [Leroy et al. \(2008\)](#) to specify the stellar velocity dispersion in the z direction, $\sigma_{*,z}$ from R_d and the local stellar surface mass density Σ_s which is obtained from Σ_R after applying eq. 4.

As noted in [Meurer et al. \(2013\)](#), a constant Q disk dominated by gas in the outskirts of galaxies where the rotation curve is flat should have $\Sigma_g(R) \propto R^{-1}$. The corresponding integrated gas content is not finite unless the distribution is truncated. Here we truncate the disks at the radius where the orbital time $t_{\text{orb}} = 2\pi R/V_c(R) = 1$ Gyr, following the work of [Meurer et al. \(2014\)](#) on the relationship between V_c and maximum radius in galaxies including the SINGG and SUNGG sample.

The total gas radial profile Σ_g is apportioned to molecular and atomic components using models for the molecular to atomic ratio

$$R_{\text{mol}} \equiv \Sigma_{\text{H}_2}/\Sigma_{\text{HI}} \quad (8)$$

Following [Zheng et al. \(2013\)](#), we test two different prescriptions for R_{mol} , both of which were also trialled by [Leroy et al. \(2008\)](#). The first is a purely empirical scaling of the stellar surface mass density (Σ_*) where

$$R_{\text{mol},s} = \frac{\Sigma_*}{81 M_\odot \text{pc}^{-2}}. \quad (9)$$

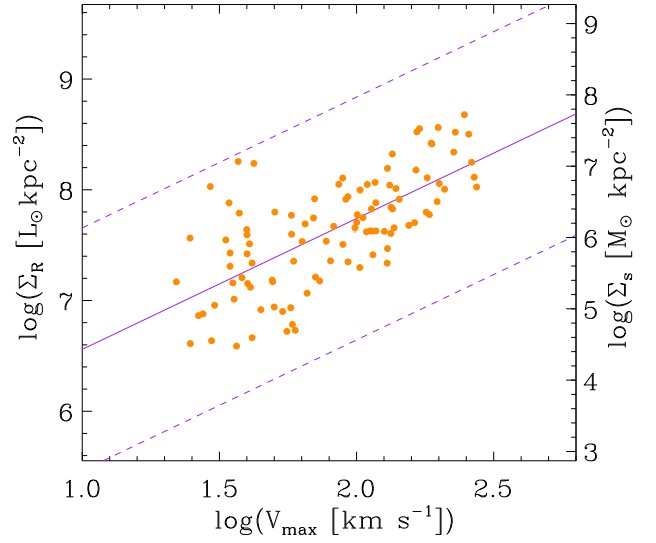


Figure 3. The observed relationship between R -band effective surface brightness Σ_R and rotation velocity amplitude for SINGG galaxies. An ordinary least squares fit to the data, is shown as the solid line. The dashed lines are offset by $\pm 2\sigma_\Sigma$ from the fit, where σ_Σ is the dispersion about the fit. The right axis shows the approximate stellar mass density, Σ_s .

The other depends upon the hydrostatic pressure, P_h , and is

$$R_{\text{mol},p} = \left(\frac{P_h}{1.7 \times 10^4 \text{ cm}^{-3} K k_B} \right)^{0.8}, \quad (10)$$

where k_B is the Boltzmann constant and P_h is given by [Elmegreen \(1989\)](#) as

$$P_h = \frac{\pi}{2} G \Sigma_g (\Sigma_g + \frac{\sigma_g}{\sigma_{*,z}} \Sigma_*), \quad (11)$$

where $\sigma_{*,z}$ is the vertical stellar velocity dispersion.

The radial profile of star formation Σ_{SFR} is calculated using an SFL that depends only on the molecular gas content Σ_{H_2} . [Bigiel et al. \(2008\)](#) used data on normal spiral and dwarf galaxies from the THINGS survey to show that in the bright part of galaxies a linear molecular SFL holds: $\Sigma_{\text{SFR}} \propto \Sigma_{\text{H}_2}$. They find the ratio between the two $\Sigma_{\text{SFR}}/\Sigma_{\text{H}_2} = \text{SFE}_{\text{H}_2} = 5.25 \times 10^{-10} \text{ yr}^{-1}$. [Zheng et al. \(2013\)](#) used a subset of the same data and a different algorithm to fit a uniform linear molecular SFL and find $\text{SFE}_{\text{H}_2} = 8.66 \times 10^{-10} \text{ yr}^{-1}$. [Bigiel et al. \(2008\)](#) show that their linear molecular SFL is well calibrated only over 1.5 dex in gas density: $\log(\Sigma_{\text{H}_2}/(1 M_\odot \text{pc}^{-2})) = 0.5$ to 2.0. While this range covers the range of gas densities typically seen in normal star forming galaxies, they show in their Fig. 15 that the linear molecular SFL underpredicts Σ_{SFR} in starburst galaxies (as observed by [Kennicutt 1998](#)) which have $\text{SFE}_{\text{H}_2} \sim 6.0 \times 10^{-9} \text{ yr}^{-1}$ and typically significantly higher Σ_{H_2} compared to normal galaxies. Therefore, we adopt an SFL that transitions between a low SFE_{H_2} , set at the value found by [Zheng et al. \(2013\)](#), and a more efficient SFE_{H_2} set at the value implied by the [Kennicutt \(1998\)](#) starburst data. The transition occurs at $\log(\Sigma_{\text{H}_2}/(1 M_\odot \text{pc}^{-2})) = 2.5$ and we use the arctan function as a convenient form to transition between the cases. The exact functional form we employ is

$$\Sigma_{\text{SFR}} = 8.66 \times 10^{-4} \Sigma_{\text{H}_2} 10^{0.84(\arctan(5(\log(\Sigma_{\text{H}_2}) - 2.5))/\pi + 0.5)}, \quad (12)$$

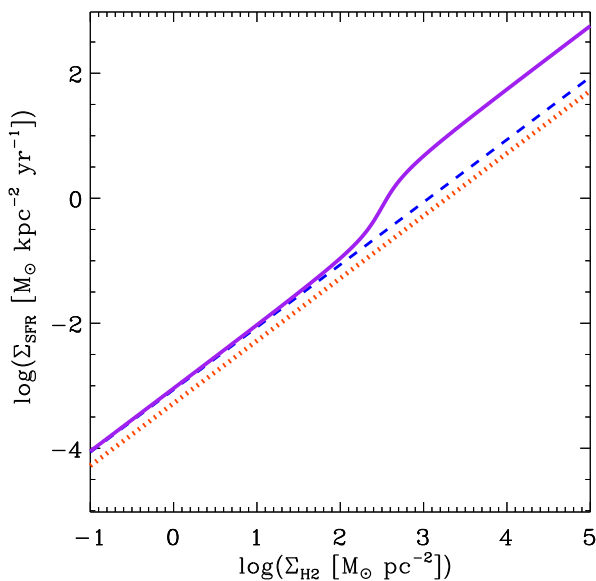


Figure 4. Our adopted molecular Star Formation Law, eq. 12 is shown as the purple (solid) line. The linear molecular SFLs of Bigiel et al. (2008) and Zheng et al. (2013) are shown by the dotted orange and dashed blue lines, respectively.

Where Σ_{SFR} is in units of $M_{\odot} \text{ kpc}^{-2} \text{ yr}^{-1}$ and Σ_{H_2} is in units of $M_{\odot} \text{ pc}^{-2} \text{ yr}^{-1}$, and includes contributions from helium and heavy elements. Fig. 4 plots this SFL in comparison to the linear molecular SFLs of Bigiel et al. (2008) and Zheng et al. (2013). The asymptotic linear behavior of this SFL at normal and high densities yields molecular gas consumption times of 1.2 Gyr and 0.17 Gyr respectively.

2.3 Model demonstration

To illustrate the behaviour of our constant- Q disk models, we show in panels (a) and (b) of Figure 5 the HI and H₂ gas densities (Σ_{HI} , Σ_{H_2}) of our models for a low- and a high-mass galaxy. The left panels (a and c) of Figure 5 represent the models for a low-mass disk galaxy with a maximum circular velocity (v_{max}) of 60 km s⁻¹. The right panels (b and d) show a Milky Way analogue galaxy having $V_{\text{max}} = 220 \text{ km s}^{-1}$, close to the highest V_{max} in our model sequence. The models for the stellar mass density and hydrostatic pressure prescriptions for R_{mol} (section 2.1) are shown with green and blue lines, respectively.

In general, it appears that the stellar surface density R_{mol} prescription is unable to convert the HI to H₂ at large radii where the stellar surface densities are low. This is especially obvious in the case of the low-mass disk galaxy and at large disk radii for both low- and high-mass disk galaxies. These results of star formation at low gas densities are consistent with the observations of galaxies with extended UV (XUV) disks (Thilker et al. 2007) where star formation in the outer low-density regions is more common than expected, based upon our understanding of star formation within the established stellar disk.

The bottom row panels of Figure 5 (panels (c) and (d)) show

the resulting SFE_{HI} at a given radius (local) and the global SFE_{HI} interior to a radius (integrated) for our models of the low- and high-mass disk galaxies. Our modelled local SFE_{HI} radial profiles are consistent with recent observations of nearby galaxies whereby the radial profiles of SFE flatten in the outer parts of galaxies at much lower values than those in the optical disks (e.g. Yim & van der Hulst 2015). At large radii, the integrated SFE_{HI} for both low- and high-mass disk models using the hydrostatic disk pressure molecular gas fraction prescription are very close to the mean SFE_{HI} found in our sample (as shown by the grey line in panels (c) and (d)). While both R_{mol} prescriptions result in very similar integrated SFE_{HI} for the model of the high-mass disk galaxy, this is not the case for the model of the low-mass disk where the stellar surface density prescription underpredicts the observed integrated SFE_{HI} .

Previous studies of star formation rates (and efficiencies) with stellar surface densities are likely to be biased towards galaxies and portions of galaxies with high molecular gas and stellar densities (e.g. Wong et al. 2013; Leroy et al. 2008) due to optical/UV and molecular gas observational limits. As such, only a narrow range of stellar surface densities (which trace the hydrostatic disk pressure) is studied.

3 SAMPLE AND OBSERVATIONS

We obtain our sample of nearby star-forming galaxies from the Survey for Ionization in Neutral Gas Galaxies (SINGG; Meurer et al. 2006) and the Survey of Ultraviolet emission of Neutral Gas Galaxies (SUNGG; Wong 2007; Wong & Meurer 2016)—two surveys which imaged an HI-selected sample of galaxies from the HI Parkes All-Sky Survey (HIPASS; Meyer et al. 2004; Zwaan et al. 2004; Koribalski et al. 2004; Wong et al. 2006) in the optical and the ultraviolet wavelengths. The size of the sample used in this paper is a factor of seven greater than that used in Meurer et al. (2013) and Zheng et al. (2013) and spans a larger range of star-forming galaxies in size and brightness (see Figure 6). The optical R -band and H α imaging for SINGG were primarily obtained from the 1.5-m telescope at the Cerro Tololo Inter-American Observatory in Chile, while the Galaxy Evolution Explorer (GALEX) satellite telescope is used to obtain the far- and near-ultraviolet (FUV and NUV) for SUNGG at 1524-Å and 2273-Å, respectively.

The sample overlap between SINGG and SUNGG consists of 306 nearby galaxies. We adopt as our sample the subset of those where (a) the 15 arcmin HIPASS beam contains only one associated star forming galaxy, and (b) the optical major to minor axial ratio is $a/b > 1.6$. Multiple and face-on galaxies are thus excluded so that v_{max} can be more accurately estimated from the HI line width.

Table 1 lists the properties of the 84 galaxies used in this paper. The distances are from Meurer et al. (2006) and mostly calculated from their recessional velocities (following Mould et al. 2000). They range from 3.3 Mpc to 112 Mpc with a median of 13 Mpc. Figure 7 presents the HI and stellar mass distributions for our HI-selected sample of star-forming galaxies. Distinct from optically-selected samples of star forming galaxies, we do not propagate a bias against star-forming galaxies with low stellar masses and/or low stellar surface brightnesses. We note that approximately half of our sample have stellar masses below $10^9 M_{\odot}$, where there is an increased scatter in both the Tully-Fisher relationship and the V_{max} and Σ_R relationship described in Section 2.2.

In this paper, we use the FUV emission from SUNGG as the tracer of the current star formation rate. The FUV emission is sen-

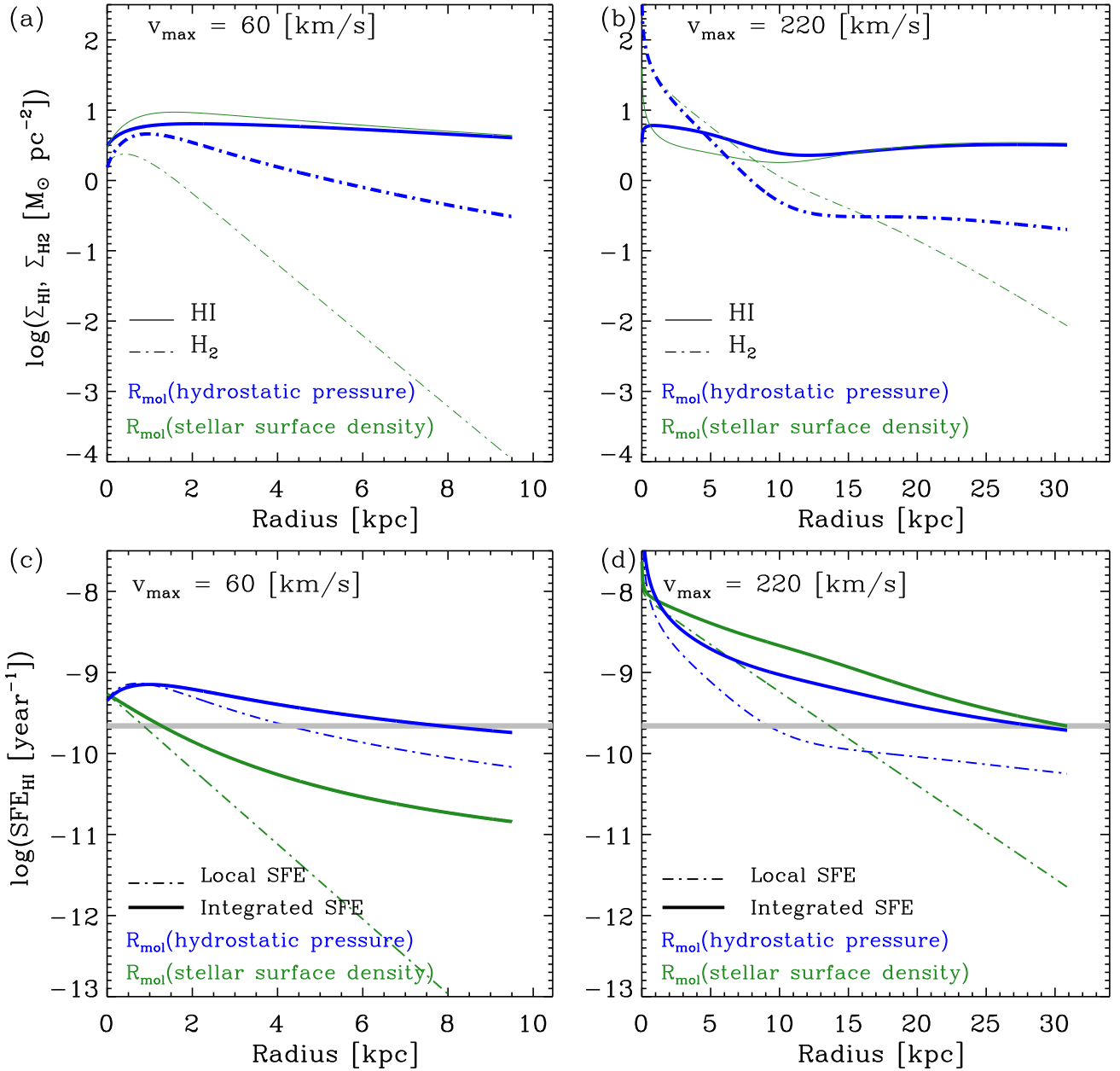


Figure 5. Panels (a) and (b) show the gas surface mass density as a function of radius for two constant- Q disk models: (a) a dwarf galaxy with a maximum circular velocity of 60 km s^{-1} ; and (b) a massive disk galaxy with a maximum circular velocity of 220 km s^{-1} . The atomic H I gas density (Σ_{HI}) is represented by the solid lines and the molecular H₂ gas density (Σ_{H_2}) is represented by the dot-dash lines. The models using the molecular gas ratio (R_{mol}) estimated via the stellar mass surface density are shown in green, and those using R_{mol} estimated via hydrostatic pressure arguments are shown in blue. Panels (c) and (d) show the local SFE_{HI} (dot-dashed lines) and integrated SFE_{HI} within the specified radius (solid lines) for our models. To guide the eye, we show the mean SFE_{HI} ($\log(SFE_{\text{HI}}) = -9.65$) found from our sample as a thick grey horizontal line.

sitive to the presence of O and B stars ($M_* > 3 M_{\odot}$). The other commonly-used star formation indicator is the $H\alpha$ emission which is sensitive to O stars ($M_* > 20 M_{\odot}$). However, the ratio between FUV and $H\alpha$ can vary between galaxies which may indicative of a varying initial mass function (IMF) or that the UV escape fraction may be different in low surface brightness and low mass galaxies (Meurer et al. 2009; Lee et al. 2009). Lee et al. (2009) argue that the FUV emission is a more accurate tracer of the true star forma-

tion rate than the $H\alpha$ emission. In this paper, we calculate the star formation rates from the FUV emission following

$$SFR(FUV) = \frac{l_{\text{FUV}}}{1.37 \times 10^{32} \text{ W } \text{\AA}^{-1}} \quad (13)$$

which is eq. 2 of Meurer et al. (2009) adjusted for consistency with a Kroupa (2001) IMF.

The optical and UV magnitudes and luminosities have been corrected for both Galactic and internal dust extinction. We have

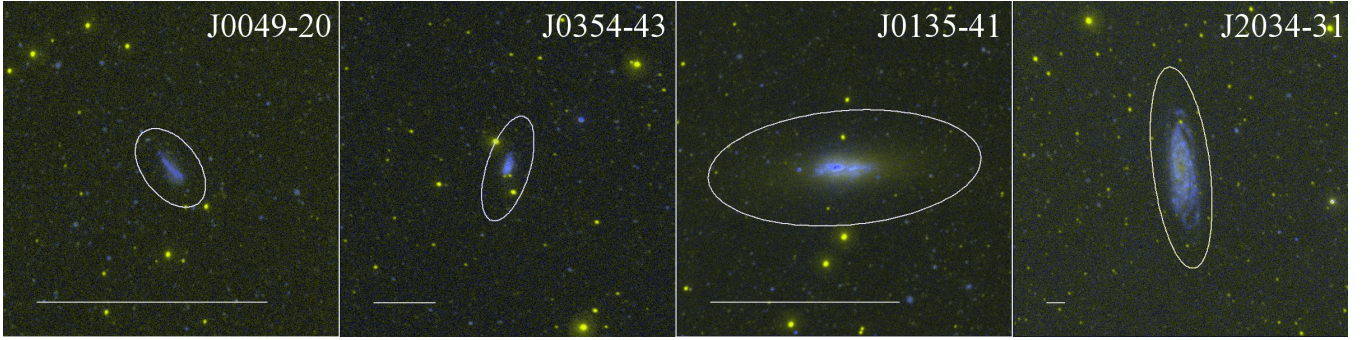


Figure 6. Four galaxies representing the variety in size and stellar surface brightness of the star-forming galaxies from the SUNGG survey. GALEX three-colour 15 arcminute by 15 arcminute postage stamps of the SUNGG UV observations where the FUV and NUV are represented by the blue and yellow, respectively. The RGB colour scaling of these images are shown by Gil de Paz et al. (2007) where blue, green and red represents the FUV, linear combination of FUV&NUV emission and NUV emission (as per Gil de Paz et al. (2007)); respectively. The scale bar represents 10 kiloparsecs.

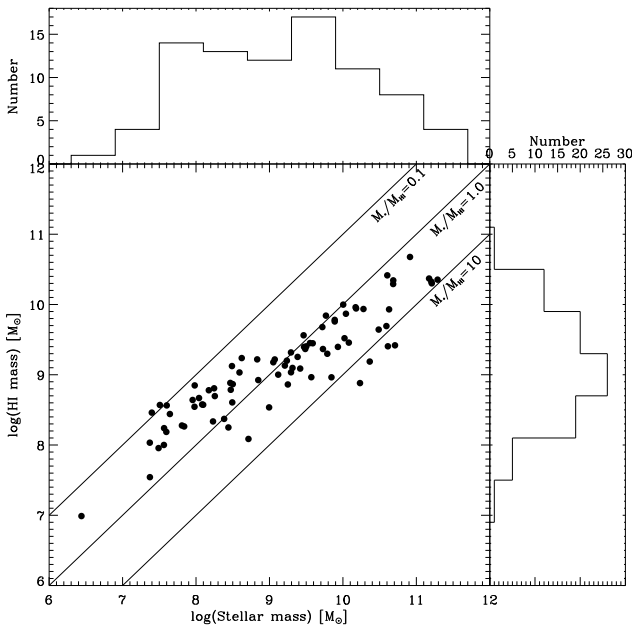


Figure 7. The HI and stellar mass distributions of our sample. The solid lines are lines of constant stellar-to-HI mass fractions ranging from 0.1 to 10.

used the internal FUV attenuation correction method derived by Salim et al. (2007) for a sample of low-redshift galaxies. The internal dust absorption correction for the optical observations are calculated empirically, based on the R -band luminosity (Meurer et al. 2006; Helmboldt et al. 2004).

3.1 The effect of the internal dust corrections on the SFE_{HI}

Although the FUV emission is a well-established tracer of recent star formation, the FUV emission is highly susceptible to dust extinction and may artificially influence the observed range of SFE_{HI} . Figure 8 compares the SFE_{HI} as a function of circular velocity with and without internal dust extinction in Panels (a) and (b), respectively. The standard deviation of the scatter in SFE_{HI} in panels (a) and (b) are very similar with log values of 0.28 and 0.29, respectively.

The omission of the dust extinction correction (as seen in Figure 8b) results in SFE_{HI} which are on average 3.8 times lower than the average dust-corrected SFE_{HI} for our sample. This implies that on average, only $\sim 26\%$ of the FUV emission escapes from the galaxies. While it is clear that the application of internal dust corrections have renormalised the SFE_{HI} , the constancy and scatter of the SFE_{HI} is not significantly reduced by these dust corrections. In Figure 8 the colour of each data point shows the internal FUV dust correction A_{FUV} . A_{FUV} correlates with V_{max} , we also find a weak correlation of A_{FUV} with SFE_{HI} . These are both expected - galaxies with more mass and more star formation tend to be dustier.

4 STAR FORMATION EFFICIENCY IN NEARBY GALAXIES

Figure 8a presents the star formation efficiencies of our sample galaxies as a function of the circular velocity (V_{max}). Our sample have an mean and median $\log(SFE_{\text{HI}})$ of -9.65 and -9.81 , respectively, as well as a standard deviation of 0.28 dex. In comparison, the stellar mass-selected GASS survey finds a constant SFE_{HI} of $10^{-9.5} \text{ year}^{-1}$ (Schiminovich et al. 2010), while the average $\log(SFE_{\text{HI}})$ from ALFALFA is $\log(SFE_{\text{HI}}) = -9.95$ (Huang et al. 2012).

Table 1: Properties of our sample.

HIPASS galaxy	Distance	v_{MAX}	M_{R}	$\log \Sigma_{\text{R}}$	$\log(SFE_{\text{HI}})$
J0008-59	112.1	216.	-22.5	7.73	-10.10
J0014-23	7.0	106.	-19.2	7.33	-9.96
J0039-14a	20.6	45.	-19.3	8.11	-9.53
J0043-22	4.9	24.	-14.7	6.89	-9.72
J0047-09	19.1	74.	-17.8	7.13	-10.06
J0047-25	3.9	209.	-21.8	8.02	-9.28
J0049-20	3.3	21.	-12.8	6.72	-9.94
J0052-31	22.9	173.	-22.0	8.31	-10.17
J0135-41	4.1	40.	-17.6	7.71	-9.57
J0145-43	4.4	38.	-16.2	6.96	-9.06
J0256-54	7.1	63.	-17.4	6.65	-10.44
J0307-31	66.9	189.	-21.8	7.54	-10.13
J0309-41	12.9	77.	-18.4	7.08	-9.72
J0310-33	15.3	61.	-17.0	6.86	-10.08
J0317-37	13.5	27.	-14.7	7.53	-9.87
J0320-52	7.0	43.	-17.0	7.52	-9.53
J0328-08	17.4	129.	-20.1	7.47	-10.05
J0331-51	14.3	133.	-20.0	8.04	-9.15
J0333-50	8.1	66.	-17.1	7.46	-9.80
J0344-44	15.9	202.	-21.0	7.86	-10.02
J0345-35	10.8	39.	-14.8	6.55	-10.32
J0349-48	13.1	133.	-18.9	7.22	-9.90
J0354-43	12.3	53.	-15.2	7.13	-9.47
J0355-40	10.5	44.	-15.0	7.30	-9.95
J0355-42	11.2	120.	-19.0	7.95	-9.62
J0404-54	15.9	186.	-20.9	8.05	-9.23
J0406-21	12.8	90.	-19.5	7.92	-9.70
J0411-35	11.4	43.	-15.6	7.37	-9.89
J0421-21	12.4	96.	-18.8	7.24	-9.81
J0429-27	13.0	44.	-16.9	7.44	-9.08
J0451-33	16.2	104.	-18.7	7.60	-9.58
J0459-26	10.0	118.	-19.2	7.51	-9.81
J0505-37	16.7	169.	-22.0	8.28	-8.96
J0506-27	17.8	43.	-17.8	7.55	-9.96
J0506-31	10.9	40.	-18.2	8.16	-9.31
J0510-36	14.1	86.	-18.8	7.56	-9.72
J0515-41	14.5	84.	-17.3	7.28	-10.30
J0516-37	18.7	140.	-19.8	7.51	-10.05
J0533-36	18.4	116.	-19.8	7.68	-9.65
J1002-06	9.7	64.	-15.9	6.84	-10.05
J1017-03	19.4	105.	-18.7	7.67	-9.70
J1046+01	12.2	118.	-18.3	7.31	-9.89
J1051-19	31.0	133.	-20.1	7.31	-9.94
J1105-00	8.6	248.	-21.7	8.45	-9.34
J1107-17	11.9	68.	-15.7	7.64	-9.70
J1110+01	11.4	41.	-15.2	7.16	-10.10
J1127-04	10.6	43.	-15.1	7.11	-9.86
J1153-28	24.4	137.	-20.4	7.44	-9.82
J1205-14	20.4	138.	-20.6	7.65	-9.67
J1217+00	8.9	32.	-15.0	6.60	-9.98
J1231-08	11.1	121.	-19.4	7.75	-9.26
J1232+00b	10.6	154.	-20.4	7.30	-9.78
J1232-07	10.5	137.	-19.2	7.72	-9.66
J1235-07	10.4	95.	-16.6	7.38	-10.01
J1253-12	8.6	44.	-16.1	7.07	-9.92
J1255+00	15.3	116.	-19.1	7.51	-9.47
J1303-17b	7.7	56.	-17.1	6.83	-10.16

Continued on next page

Table1 – continued from previous page

HIPASS galaxy	Distance	v_{MAX}	M_{R}	$\log \Sigma_{\text{R}}$	$\log(SFE_{\text{HI}})$
J1304-10	47.4	266.	-23.4	7.91	-9.51
J1329-17	22.1	257.	-21.8	7.60	-9.67
J1423+01	22.5	121.	-19.4	7.50	-9.62
J1447-17	33.5	109.	-20.8	7.57	-9.65
J1500+01	22.5	191.	-21.2	8.21	-9.12
J1558-10	14.8	53.	-16.4	7.74	-10.24
J2009-61	11.2	62.	-17.1	7.28	-10.04
J2034-31	41.9	259.	-23.2	8.18	-9.45
J2044-68	45.4	230.	-23.1	8.02	-9.58
J2052-69	7.5	92.	-18.6	7.40	-9.72
J2127-60	24.9	146.	-20.8	7.73	-9.69
J2129-52	12.3	81.	-18.3	7.44	-9.85
J2135-63	45.2	233.	-23.2	8.19	-9.32
J2136-54	12.0	102.	-20.2	7.50	-9.40
J2214-66	24.8	184.	-20.5	7.63	-10.39
J2217-42	32.1	29.	-16.0	6.81	-10.26
J2220-46	13.2	106.	-19.9	7.15	-10.04
J2234-04	14.1	53.	-16.6	7.12	-10.12
J2235-26	21.1	167.	-21.5	7.96	-9.53
J2239-04	13.2	33.	-16.0	6.90	-9.86
J2254-26	12.3	74.	-16.2	7.86	-10.04
J2257-42	13.4	59.	-17.0	6.65	-10.13
J2302-40	15.3	95.	-19.9	7.77	-9.52
J2326-37	10.0	37.	-16.5	7.37	-9.77
J2337-47	40.8	277.	-22.0	7.78	-10.30
J2349-37	9.2	45.	-15.3	6.62	-10.18
J2352-52	7.7	24.	-15.1	7.13	-9.88

Column 1: The HIPASS identification of the galaxy. Column 2: Distances in megaparsecs. Column 3: Circular velocity in km s^{-1} . Column 4: Dust-corrected optical *R*-band absolute magnitude. Column 5: Effective *R*-band surface brightness density in $L_{\odot} \text{ kpc}^{-2}$. Column 6: Log of HI-normalised *SFE*.

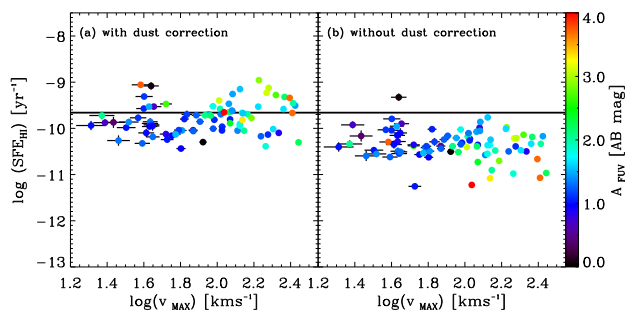


Figure 8. Effect of internal dust extinction on the measured SFE_{HI} in our sample. Panel (a) shows the integrated SFE_{HI} with internal dust correction as a function of v_{MAX} and panel (b) shows the integrated SFE_{HI} without dust correction as a function of v_{MAX} . The horizontal line marks the mean SFE_{HI} of our sample. The data points are coloured according to the internal dust correction as shown on the colour bar on the right of the figure.

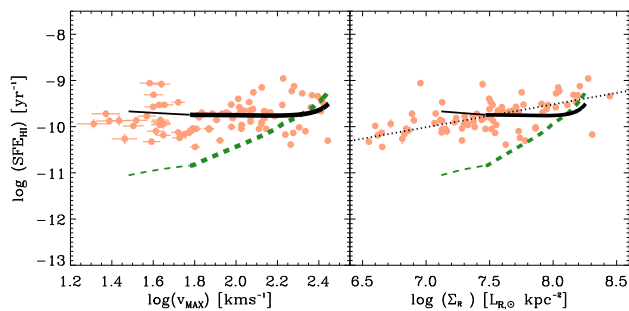


Figure 9. The H I star formation efficiency as a function of circular velocity (v_{MAX}) and the effective R -band surface brightness (Σ_R). The solid black line represents our model where R_{mol} is dictated by the hydrostatic pressure (P_h) and the dashed green line represents our model where the R_{mol} depends on the stellar surface density (Σ_*). We note that the rotation curves used in our models are calibrated to observations only for V_{MAX} covering the range of 60 km s^{-1} to 280 km s^{-1} . The thinner line extensions to lower V_{MAX} are extrapolations of our disk models’ predictions for galaxies with V_{MAX} between 30 to 60 km s^{-1} .

4.1 Comparison with stable disk models

In Figure 9 we compare the observed global SFE_{HI} for our sample of nearby star-forming galaxies to those predicted by our stable disk models (as described in Section 2). The predicted SFE_{HI} from our stable disk models are in good agreement to those found for our sample of nearby star-forming galaxies. This is especially the case for our model which uses the hydrostatic pressure prescription for R_{mol} (equation 10). We find a mean $\log(SFE_{\text{HI}}) = -9.71$ and a standard deviation of 0.02 dex for our stable disk model which uses the P_h R_{mol} prescription. This mean SFE_{HI} is evaluated individually for each modelled galaxy with V_{MAX} between 60 and 280 km s^{-1} in increments of 0.4 km s^{-1} . While both R_{mol} prescriptions yield similar global SFE_{HI} for galaxies similar in mass to the Milky Way (see Figure 5d & Figure 9), the stellar mass density prescription (equation 9) for R_{mol} predicts that the SFE_{HI} should correlate strongly with V_{MAX} , which is not observed.

If we extend our models to above our current limit of $V_{\text{MAX}} = 280 \text{ km s}^{-1}$, we find sharply rising rotation curves, presumably from a strong bulge, resulting in large gas densities required to maintain a constant Q and thus high star formation intensity (ie.

starburst). Consequently, a sharply rising SFE_{HI} with V_{MAX} would result for our models for $V_{\text{MAX}} > 280 \text{ km s}^{-1}$. This suggests that either a stable disk cannot be maintained in the central regions of high-mass galaxies (Zheng et al. 2013); or that high mass galaxies have already exhausted their central gas repositories through previous starburst activity. We note that for a $V_{\text{MAX}} \leq 280 \text{ km s}^{-1}$ limit, the resulting SFE_{HI} differs very little from our standard model sequence if we replace our adopted star formation law with the linear molecular star formation law of Zheng et al. (2013). This is because the required gas densities are typically barely high enough to invoke the “starburst” component of our adopted star formation law, and then only in the central regions of models at the highest V_{MAX} values. The “starburst” component becomes more relevant for our low angular momentum model (discussed later in this section) and our models of $z = 2$ galaxies (see Section 5.3).

Within our sample, we do not have any galaxies with $V_{\text{MAX}} > 280 \text{ km s}^{-1}$; they are rare in the Local Universe. As noted in Section 2.1, such galaxies are beyond the range of properties used to calibrate the Universal Rotation Curve, hence it is not clear that such an extrapolation produces a realistic rotation curve. Our sample selection excludes galaxies with star-forming companions which may further decrease the probability of our sample including galaxies with high V_{MAX} . In addition, higher mass systems in the Local Universe are redder and forming less stars (e.g. Kauffmann et al. 2003) and hence, not expected to possess large reservoirs of H I.

While the rotation curve model used is not calibrated for galaxies with $V_{\text{MAX}} < 60 \text{ km s}^{-1}$, the extrapolation of our model (which uses the P_h R_{mol} prescription) to lower V_{MAX} continues to be in good agreement with our observations (see Figure 9). This suggests that the universal rotation curve model adequately accounts for the true rotation curves of dwarf galaxies.

Our sample of nearby star-forming galaxies show a positive correlation between SFE_{HI} and the R -band surface brightness, Σ_R . A robust linear fit results in a positive slope of 0.50 and an RMS scatter about this fit of 0.23 dex and a Pearson R -correlation coefficient of 0.55 . Relative to our stable disk models, this correlation has a slope which is less steep than the disk model which uses the Σ_* R_{mol} prescription (slope of 1.94). While the disk model which uses the P_h R_{mol} prescription predicts a better fit to the data, the predicted slope is -0.03 .

4.2 Variations in the intrinsic surface brightness distribution

The positive correlation between Σ_R and SFE_{HI} suggests that a second parameter is at play. Since the primary parameter of our model is V_{MAX} , a proxy for total mass, an obvious choice for the second parameter is the spin or angular momentum of the disk. For a given V_{MAX} , a low angular momentum disk will appear more concentrated and hence have a higher surface brightness relative to a high angular momentum disk. The rotation curve will reach the same V_{MAX} but have a steeper rise in the centre. In the context of our model this results in an increased central star formation rate, but relatively little change in the H I content, and hence a higher SFE_{HI} for a given V_{MAX} . Figure 2 shows that the V_{MAX} -surface brightness correlation has a scatter of 0.3 dex in Σ_R . This is equivalent to a scatter of 0.15 dex in scale length, or a factor of 1.4 for pure exponential disks at fixed luminosity.

To test the effects of angular momentum on our models, we expanded and contracted the scale length of the disk surface mass distribution, the rotation curve, and the truncation radius while keeping the luminosity and V_{MAX} fixed in our models. Figure 10 shows

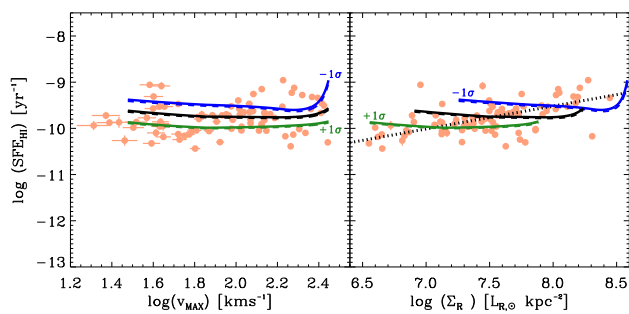


Figure 10. The data in these two panels is the same as in Figure 8. Here, the solid lines represent our model where R_{mol} is dictated by the hydrostatic pressure (P_h) and the dotted line marks the positive correlation between stellar surface brightness and SFE_{HI} . The middle solid line (black) correspond to our default model as shown in Figure 9. The top and bottom solid lines correspond to the -1σ and $+1\sigma$ variation in the linear scale lengths at fixed stellar luminosities and V_{max} , respectively. **The dashed lines represent the model with a simple linear molecular star formation law as per Zheng et al. (2013).**

another version of Figure 9 where the P_h prescription for R_{mol} are plotted in lines of three different thicknesses and colours to represent three variations in our model’s surface brightness distribution. The default surface brightness distribution used in this paper (represented by the black line in Figure 9) is also represented by the black solid line of intermediate thickness in Figure 10. The green and blue solid lines in Figure 10 represent $\pm 1\sigma$ variations in the surface brightness distributions versus V_{max} relationship. We note that the scatter in the R_{max} versus V_{max} relationship from which we derive the constant orbital time is ≈ 0.16 dex. Therefore, the scatter in both relationships are consistent with being driven by the scatter in the scale size. In addition, we show in Figure 10 that the differences are not significant between the models that use the star formation law described in Section 2.2 (solid lines) or the linear molecular star formation laws (dashed lines) as per Zheng et al. (2013).

As can be seen in the right panel of Figure 10, by varying the scale length by 0.15 dex and using our P_h prescription for R_{mol} we produce model lines that are shifted diagonally in the SFE_{HI} versus Σ_R plane and encompass the envelope of observed data points³. Therefore, we posit that the observed correlation between the stellar surface density and SFE_{HI} is due to an intrinsic variation in the underlying scale length and hence disk angular momentum of the galaxies.

5 DISCUSSION

5.1 Varying the initial assumptions of our model

We examine the robustness of the assumptions and empirical correlations used in our models by investigating the resulting effects when each of these assumptions are varied. We show in this subsection that our results remain unchanged and are robust against the uncertainties that exist within the assumptions made and empirical correlations used in our model. Our variation of our initial

³ We also examined the effects of varying scale length on the Σ_* prescription for R_{mol} . As in the fiducial model, none of the Σ_* prescription models fit the data points, so we do not show the results here so as not to clutter the figures.

Table 2. Comparison of the observed mean SFE_{HI} with the mean values of the various models tested in Section 5.1.

Sample	$\log(\text{mean } SFE_{\text{HI}}) [\text{yr}^{-1}]$
Observations	$-9.65 (\pm 0.28)$
Default model	-9.71
$Q_{\text{sg}} = 1.3$	-9.47
$Q_{\text{sg}} = 1.9$	-9.83
$\sigma_g = 8 \text{ km s}^{-1}$	-9.89
$\sigma_g = 20 \text{ km s}^{-1}$	-9.58
1σ -brighter TFR	-9.65
1σ -fainter TFR	-9.58

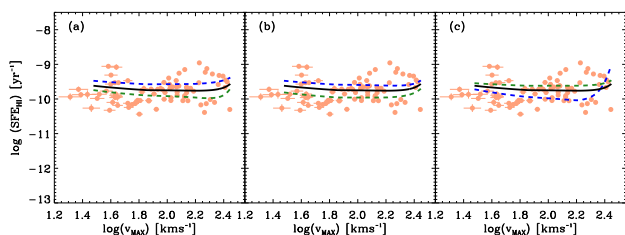


Figure 11. The data in these two panels is the same as in Figure 8. Here, the black solid lines in all 3 panels represent the default model where R_{mol} is dictated by the hydrostatic pressure (P_h) as in Figure 9. Panel (a) shows alternative models which assume constant $Q_{\text{sg}} = 1.3$ (blue dashed line) and constant $Q_{\text{sg}} = 1.9$ (green dashed line). Panel (b) shows alternative models which assume $\sigma_{\text{rmg}} = 14 \text{ km s}^{-1}$ (blue dashed line) and $\sigma_{\text{rmg}} = 8 \text{ km s}^{-1}$ (green dashed line). Panel (c) shows alternative models which adopt Tully-Fisher relationships which differ by the 1σ scatter in Figure 2. The models which adopt a Tully-Fisher relationship that is 1σ brighter and 1σ fainter are represented by the blue dashed line and the green dashed line, respectively.

assumptions within known constraints result in models which are still consistent within the scatter of our observations. We specifically examine the effects of varying 3 key parameters of our models, namely: a) the value of the assumed constant Q_{sg} ; b) the gas velocity dispersion, σ_g ; and c) the zero point in the Tully-Fisher relationship. Table 2 lists the observed mean SFE_{HI} of our sample, the mean SFE_{HI} of our default model, and the mean SFE_{HI} of the model sequence when each of these parameters are adjusted.

Recent studies such as Zheng et al. (2013) have measured the radial profiles of the Toomre Q_{sg} in samples of nearby galaxies and have determined that the Q_{sg} values within the disks of galaxies are constant with an average Q_{sg} of 1.6. However, the standard deviation of the derived Q_{sg} for the Zheng et al. (2013) sample is 0.3 excluding the 2 largest outliers in their sample. Both outliers in the Zheng et al. (2013) sample have $Q_{\text{sg}} > 2.0$ and consist of a dwarf galaxy and a very massive galaxy with V_{max} of 50 km s^{-1} and 300 km s^{-1} , beyond the range of the V_{max} used in the family of rotation curves adopted in this paper.

Figure 11a illustrates the effect of varying the assumed constant Q_{sg} in our models by $\pm 1\sigma$. Increasing to $Q_{\text{sg}} = 1.9$ results in a lower gas content. The molecular phase and therefore the star formation rate is more suppressed than the atomic phase resulting in a lower SFE_{HI} . The converse is true if we decrease the stability parameter to $Q_{\text{sg}} = 1.3$.

Our adopted constant gas velocity dispersion of 11 km s^{-1} is based upon the mean dispersion measurements from the THINGS

HI second-order moment maps (Leroy et al. 2008; Tamburro et al. 2009; Zheng et al. 2013). The 1σ scatter of these measurements is 3 km s^{-1} . We show in Figure 11b that a model which assumes a larger gas velocity dispersion results in a higher SFE_{HI} than one which assumes a lower gas velocity dispersion. This is because increasing the velocity dispersion allows more gas to be packed in to a disk to get the same Q_{sg} , and a larger fraction ends up molecular and thus star forming. The uniformity of the resulting SFE_{HI} as a function of V_{max} is preserved regardless of the assumed velocity dispersion.

Figure 11c shows the model results for when we vary the assumed Tully-Fisher relationship by 1σ of the observed scatter in Figure 2. The model which adopts the Tully-Fisher relationship that is 1σ brighter (blue dashed line) shows a general suppression in SFE_{HI} because the brighter Tully-Fisher relationship results in higher stellar masses relative to the mean fitted relationship used. Our constant Q_{sg} model subsequently balances out the increase in stellar component with a decrease in the gas component. The effect on SFE_{HI} depends on which phase of the ISM is most affected. For $V_{\text{max}} \lesssim 220 \text{ km s}^{-1}$ SFE_{HI} is less than the default model because the molecular phase is more suppressed than the atomic phase of the ISM. The situation reverses at larger V_{max} , with the HI phase more suppressed, resulting in an increased SFE_{HI} . Models which adopt a fainter Tully-Fisher relationship results in greater gas content at all radii, and an overall higher molecular fraction, subsequently yielding greater SFE_{HI} than that of our default model at all V_{max} .

5.2 Physical insights from our model

We see that our marginally stable disk model does a good job of accounting for the uniform SFE_{HI} of disk galaxies. In some sense, the fact that we can account for the entire sequence of disk galaxies should not be surprising since it relates other known properties of the family of star-forming galaxies such as the Tully-Fisher relation, the surface-brightness luminosity relationship, an SFL calibrated on disk galaxies, and the Persic et al. (1996) URC. The marginal stability of galaxy disks has also been known for some time (e.g. Kennicutt 1989; Leroy et al. 2008; Meurer et al. 2013). However, this is the first time it has been invoked as the primary physical basis for understanding the sequence of star forming galaxies.

We find that the P_h prescription for R_{mol} works best for explaining the uniform SFE_{HI} . Previously Leroy et al. (2008) found that an empirical scaling of R_{mol} with stellar mass density Σ_* worked marginally better than the more physically based P_h prescription. However, that study was limited to the optically bright part of galaxies and did not include the outer disks where HI becomes an important contributor to the disk mass density, and where weak star formation can often be seen, especially in the UV (Gil de Paz et al. 2007; Thilker et al. 2007). Even where the star formation intensity in such an extended gaseous disk is weak compared to the central star formation, the contribution to the total SFR can be significant. A case in point is the BCD galaxy NGC 2915, where the outer disk star formation intensity is $\sim 0.5\%$ that in the centre of this galaxy yet comprises $\sim 11\%$ of the total SFR (Bruzzeze et al. 2015; Werk et al. 2010).

Our assumed stellar mass distribution is a pure exponential disk, i.e. without a bulge. The results indicate this model is adequate. It is probable that the HI selection of our sample ensures that we do not have many bulge-dominated or early-type galaxies. The sample used to define our rotation curve model was se-

lected to have Hubble types Sb to Sd, thus avoiding the more bulge dominated Sa types (Mathewson et al. 1992). In the context of our models, there are two other reasons why bulge dominated galaxies are unlikely to contribute greatly to the URC. Firstly, the high central densities of bulge dominated disks require very high Σ_g to produce $Q = 1.6$. Consequently, the star formation in this regime will be at the starburst portion of our adopted SFL, resulting in a short gas consumption timescale, hence making these galaxies rare. Secondly, those galaxies that do manage to accrete enough gas into their centres to match our model would need to have done so quickly, i.e. through an interaction or merger. This should lead to large scale velocity field asymmetries, and galaxies with asymmetric velocity profiles were excluded from the sub-sample of galaxies used by Persic & Salucci (1995); Persic et al. (1996) to compile the URC.

The model presented here is an elaboration of our previous work on the implications of disks maintaining constant stability. In Meurer et al. (2013) we showed that the gas dominated outer disks with a constant Q in potentials with a flat rotation curve can match the observed radial Σ_{HI} distributions and gas to total mass ratio. In Zheng et al. (2013) we showed that by assuming a constant Q_{sg} , we could crudely reproduce radial profiles of HI, H₂, and Σ_{SFR} out to the traditional optical extents of galaxies given their rotation curves and stellar mass profiles. Since star formation is more centrally concentrated than HI, here we are required to consider the full radial properties of galaxies.

We note that our models have some similarities to the semi-analytic models of Lagos et al. (2011). They also used a hydrostatic pressure relationship to apportion the ISM in galaxies into molecular and atomic phases and a molecular star formation law to determine the SFR. One key difference is that they assume that Σ_g has an exponential radial profile. They allow the disk mass and scale length to evolve to accommodate the build-up of gas content and angular momentum through accretion. They are then able to reproduce a large variety of properties of disk galaxies. However, SFE_{HI} is not one of the properties that they studied. Their models are more maturely developed than ours which address neither the source of the gas nor their evolution. The strength of our model is the physical basis for the structure of the disk. Hence, it should be straightforward to adapt our model for evolutionary effects.

5.3 Application to distant newly-formed galaxies

As early as redshift $z \sim 2$, disk-dominated systems seem to be well established, albeit with higher velocity dispersions relative to galaxies in the Local Universe. Recent studies of star-forming galaxies at $z \sim 2$ have found while the morphologies appear clumpier than low- z counterparts and with higher velocity dispersions, a significant fraction of galaxies are disk-dominated and can be described by a relatively constant Q (Genzel et al. 2008; Cresci et al. 2009; Förster Schreiber et al. 2009; Genzel et al. 2014). Following the results of Förster Schreiber et al. (2009), we find an average $\sigma_g = 60 \text{ km s}^{-1}$, a median H α half light radius of 4.6 kpc, a median SFR=135 $M_{\odot} \text{ yr}^{-1}$, a median effective star formation intensity (SFR per unit projected area within the half light radius) of $0.74 M_{\odot} \text{ kpc}^{-2} \text{ yr}^{-1}$, a median $V_{\text{max}}=235 \text{ km s}^{-1}$ and a median dynamical mass of $1.4 \times 10^{11} M_{\odot}$. How do these properties compare to what we would expect for young massive disk galaxies?

To this end, we consider the properties of a Milky Way analogue, having $V_{\text{max}} = 220 \text{ km s}^{-1}$, at the early stages of its formation. Our adopted model for this V_{max} for a galaxy in the Local

Table 3. Comparison of model properties for a Milky-Way-like disk galaxy ($V_{\max}=220 \text{ km s}^{-1}$) at low- and high redshifts.

Property	$z = 0$	$z = 2$
H I effective radius	22.4 kpc	12.3 kpc
H ₂ effective radius	6.1 kpc	8.0 kpc
SFR effective radius	5.8 kpc	6.3 kpc
SFR	$1.8 M_{\odot} \text{ yr}^{-1}$	$94 M_{\odot} \text{ yr}^{-1}$
Total gas depletion time, t	6.3 Gyr	0.84 Gyr
$\log SFE_{\text{HI}}$	-9.72 year^{-1}	-7.91 year^{-1}
$\Sigma_{\text{SFR}}(R_e)$	$0.008 M_{\odot} \text{ kpc}^{-2} \text{ yr}^{-1}$	$0.377 M_{\odot} \text{ kpc}^{-2} \text{ yr}^{-1}$

Universe, presented in § 2.3, has a total baryon mass, taken to be the sum of the stellar and gas disk mass, $M_{\text{baryon}} = 8.3 \times 10^{10} M_{\odot}$, of which 18% is gas. The total gas mass is thus $1.5 \times 10^{10} M_{\odot}$ where the atomic component account for 84% of the total gas. For our young galaxy model we place this entire baryon mass in a pure gas disk having $Q = 1.6$ and $\sigma_g = 60 \text{ km s}^{-1}$. We adopt the same rotation curve model as before, and now use the familiar single fluid Q_g model to determine the Σ_g distribution. As before, we use the hydrostatic pressure prescription to apportion the gas into the atomic and molecular phases and the molecular SFL (Section 2.1) to derive the resultant radial star formation distribution. The radial profiles are truncated when the enclosed gas mass equals the above M_{baryon} (see Figure 12). We find that the gas in this high- z model would be predominantly molecular, while 10% is atomic ($M_{\text{HI}} = 8.0 \times 10^9 M_{\odot}$)—much less than that found for the low- z model.

From these radial profiles we derive an integrated SFR of $94 M_{\odot} \text{ yr}^{-1}$, a star formation half-light radius to be 6.3 kpc, and an effective star formation intensity of $0.38 M_{\odot} \text{ kpc}^{-2} \text{ yr}^{-1}$. Our modelled integrated SFR is very close to the median observed SFR of disk dominated galaxies at $z \sim 2$, while the effective star formation intensity is within the observed range of these galaxies (e.g. Johnston et al. 2015; Förster Schreiber et al. 2009). On the other hand, the size of the modelled galaxy is slightly larger than observed. Table 3 summarises the main properties found for our models.

We note that if only half of the galaxy had assembled at these high redshifts (i.e. the outer 50% of the gas mass and the resultant star formation were removed), then the galaxy model would extend out to 8.9 kpc, have a SFR of $60 M_{\odot} \text{ yr}^{-1}$, a SFR effective radius of 4.1 kpc, and an effective star formation intensity of $0.56 M_{\odot} \text{ kpc}^{-2} \text{ yr}^{-1}$. In this case all quantities are within the range observed for the $z \sim 2$ disk galaxies. Therefore, our model proto-Milky Way would have star forming properties more similar to what is observed in high-redshift young disk galaxies, if half to all of its baryons are assembled in a disk having $Q \sim 1.6$.

6 CONCLUSIONS

The sequence of star forming galaxies defined by our sample, spans five orders of magnitude in stellar mass and is unimodal. We find that the constant SFE_{HI} along this sequence can be effectively described by galaxy disks with a constant marginal stability. The primary parameter giving the structure of a galaxy in this model is the rotational amplitude V_{\max} , a proxy for the total galaxy mass. Combined with previously-known scaling relations (such as the Tully-Fisher relationship, and the surface brightness– V_{\max} relationship), we derive the distribution of the stars and dark matter.

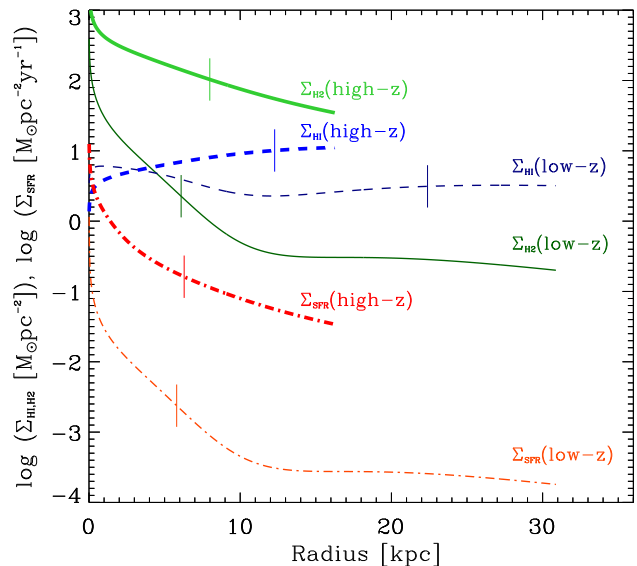


Figure 12. A comparison of the gas density and star formation intensity radial profiles of our Milky Way analogue models ($V_{\max}=220 \text{ km s}^{-1}$) at low- and high-redshifts. The H I and H₂ densities are represented by the dashed and solid lines, respectively, while the star formation intensity is represented by the dot-dash line. The thick and thin versions of each linestyle represent the high and low redshift models. The effective radius for each profile is marked by a thin vertical solid line.

The gas disk structure, the relative distribution of the gas phases and subsequently the star formation is a consequence of this framework. While the internal structure of galaxies varies greatly along the sequence, the integrated SFE_{HI} of galaxies is constant at the truncation radii of disks.

A weak correlation between the SFE_{HI} and Σ_R indicates that angular momentum is a second parameter affecting the distribution of the ISM and stars. Low specific angular momentum galaxies have shorter scale lengths and a more compact mass distribution. In the context of our models, this results in higher mass density gaseous disks and consequently, higher surface brightnesses. Similarly, lower specific angular momentum galaxies have less dense disks and less intense star formation. Our conclusions are similar to those of Popping et al. (2015) who found the overall SFE (SFR normalised by total gas) of galaxies to be primarily governed by the absolute amount of cold gas; with a secondary dependence upon the disk scale lengths.

Previous studies (e.g. Leroy et al. 2008; Wong et al. 2013) have emphasised the observed correlation between R_{mol} (and Σ_{H_2}) with Σ_* — suggesting that the local supply of molecular gas is regulated by the stellar disk of the galaxy. However the observed correlations linking Σ_* to Σ_{SFR} is not unexpected (e.g. Ryder & Dopita 1994; Dopita & Ryder 1994) because the hydrostatic pressure and the stellar surface density are strongly correlated within the optical disks of massive galaxies (e.g. Blitz & Rosolowsky 2006; Leroy et al. 2008). The fact that the observations are well-modelled with the hydrostatic pressure model suggests that it provides a better overall prescription for setting the H₂/HI ratio and hence, the HI-based SFE_{HI} . This is especially the case for dwarf galaxies where the gaseous disk (as opposed to the stellar disk) is more relevant for setting the hydrostatic pressure.

In this paper, we have also shown that our simple constant- Q model is able to reproduce the observed star formation properties of a proto-Milky Way at higher redshifts when the Universe was at its peak star formation period. Since our model is static and only deals with the disk component, we have not been able to address the effects from evolution or other common galactic structures such as bulges and bars. However, the success of our model at reproducing the observed star formation properties of low- and high-redshift galaxies suggest that star formation in galaxies is largely due to the formation and stabilisation of their disks.

Acknowledgments. Support for the work presented here was also obtained through a NASA GALEX Guest Investigator grant, GALEX GI04-0105-0009 and GALEX archival grant NNX09AF85G. Early work on the data presented here was also supported by NASA LTSA grant NAG5-13083 to G.R. Meurer. We thank the anonymous referee for their support of this paper and for improving the manuscript. This research has made use of the NASA/IPAC Extragalactic Database (NED), which is operated by the Jet Propulsion Laboratory, California Institute of Technology, under contract with the National Aeronautics and Space Administration.

REFERENCES

- Battaner E., Florido E., 2000, *Fundamentals of Cosmic Physics*, **21**, 1
- Bell E. F., McIntosh D. H., Katz N., Weinberg M. D., 2003, *ApJS*, **149**, 289
- Bigiel F., Leroy A., Walter F., Brinks E., de Blok W. J. G., Madore B., Thornley M. D., 2008, *AJ*, **136**, 2846
- Blanton M. R., et al., 2003, *ApJ*, **594**, 186
- Blitz L., Rosolowsky E., 2006, *ApJ*, **650**, 933
- Bosma A., 1981, *AJ*, **86**, 1825
- Brinchmann J., Charlot S., White S. D. M., Tremonti C., Kauffmann G., Heckman T., Brinkmann J., 2004, *MNRAS*, **351**, 1151
- Bruzze S. M., Meurer G. R., Lagos C. D. P., Elson E. C., Werk J. K., Blakeslee J. P., Ford H., 2015, *MNRAS*, **447**, 618
- Cortese L., et al., 2014, *ApJ*, **795**, L37
- Cresci G., et al., 2009, *ApJ*, **697**, 115
- Disney M., Phillipps S., 1985, *MNRAS*, **216**, 53
- Dopita M. A., Ryder S. D., 1994, *ApJ*, **430**, 163
- Driver S. P., et al., 2006, *MNRAS*, **368**, 414
- Elmegreen B. G., 1989, *ApJ*, **338**, 178
- Fisher J. R., Tully R. B., 1981, *ApJS*, **47**, 139
- Förster Schreiber N. M., et al., 2009, *ApJ*, **706**, 1364
- Freeman K. C., 1970, *ApJ*, **160**, 811
- Genzel R., et al., 2008, *ApJ*, **687**, 59
- Genzel R., et al., 2014, *ApJ*, **785**, 75
- Gil de Paz A., et al., 2007, *ApJS*, **173**, 185
- Helmboldt J. F., Walterbos R. A. M., Bothun G. D., O’Neil K., de Blok W. J. G., 2004, *ApJ*, **613**, 914
- Huang S., Haynes M. P., Giovanelli R., Brinchmann J., 2012, *ApJ*, **756**, 113
- Hunt L. K., et al., 2015, *A&A*, **583**, A114
- Johnston R., Vaccari M., Jarvis M., Smith M., Giovannoli E., Häußler B., Prescott M., 2015, *MNRAS*, **453**, 2540
- Karim A., et al., 2011, *ApJ*, **730**, 61
- Kauffmann G., et al., 2003, *MNRAS*, **341**, 54
- Kennicutt R. C., 1989, *ApJ*, **344**, 685
- Kennicutt R. C., 1998, *ARA&A*, **36**, 189
- Koribalski B. S., et al., 2004, *AJ*, **128**, 16
- Kroupa P., 2001, *MNRAS*, **322**, 231
- Lagos C. D. P., Baugh C. M., Lacey C. G., Benson A. J., Kim H.-S., Power C., 2011, *MNRAS*, **418**, 1649
- Lee J. C., et al., 2009, *ApJ*, **706**, 599
- Lehnert M. D., Le Tiran L., Nesvadba N. P. H., van Driel W., Boulanger F., Di Matteo P., 2013, *A&A*, **555**, A72
- Leroy A. K., Walter F., Brinks E., Bigiel F., de Blok W. J. G., Madore B., Thornley M. D., 2008, *AJ*, **136**, 2782
- Mathewson D. S., Ford V. L., Buchhorn M., 1992, *ApJS*, **81**, 413
- McGaugh S. S., 2005, *ApJ*, **632**, 859
- McGaugh S. S., Schombert J. M., Bothun G. D., de Blok W. J. G., 2000, *ApJ*, **533**, L99
- Meurer G. R., et al., 2006, *ApJS*, **165**, 307
- Meurer G. R., et al., 2009, *ApJ*, **695**, 765
- Meurer G. R., Zheng Z., de Blok W. J. G., 2013, *MNRAS*, **429**, 2537
- Meurer G., Obreschkow D., Hanish D., Wong O., Zheng Z., de Blok E., Thilker D. A., SINGG-SUNGG Team 2014, in *American Astronomical Society Meeting Abstracts #223*, p. 410.01
- Meyer M. J., et al., 2004, *MNRAS*, **350**, 1195
- Meyer M. J., Zwaan M. A., Webster R. L., Schneider S., Staveley-Smith L., 2008, *MNRAS*, **391**, 1712
- Mould J. R., et al., 2000, *ApJ*, **529**, 786
- Navarro J. F., Frenk C. S., White S. D. M., 1997, *ApJ*, **490**, 493
- Persic M., Salucci P., 1995, *ApJS*, **99**, 501
- Persic M., Salucci P., Stel F., 1996, *MNRAS*, **281**, 27
- Popping G., Caputi K. I., Trager S. C., Somerville R. S., Dekel A., Kassin S. A., Kocevski D. D., Koekemoer A. M. e. a., 2015, *MNRAS*, **454**, 2258
- Ryder S. D., Dopita M. A., 1994, *ApJ*, **430**, 142
- Salim S., et al., 2007, *ApJS*, **173**, 267
- Schiminovich D., et al., 2010, *MNRAS*, **408**, 919
- Simons R. C., Kassin S. A., Weiner B. J., Heckman T. M., Lee J. C., Lotz J. M., Peth M., Tchernyshyov K., 2015, *MNRAS*, **452**, 986
- Sobral D., Best P. N., Smail I., Mobasher B., Stott J., Nisbet D., 2014, *MNRAS*, **437**, 3516
- Tacconi L. J., Young J. S., 1986, *ApJ*, **308**, 600
- Tamburro D., Rix H.-W., Leroy A. K., Mac Low M.-M., Walter F., Kennicutt R. C., Brinks E., de Blok W. J. G., 2009, *AJ*, **137**, 4424
- Thilker D. A., et al., 2007, *ApJS*, **173**, 538
- Toomre A., 1964, *ApJ*, **139**, 1217
- Wang B., Silk J., 1994, *ApJ*, **427**, 759
- Werk J. K., Putman M. E., Meurer G. R., Thilker D. A., Allen R. J., Bland-Hawthorn J., Kravtsov A., Freeman K., 2010, *ApJ*, **715**, 656
- Whitaker K. E., van Dokkum P. G., Brammer G., Franx M., 2012, *ApJ*, **754**, L29
- Wong O. I., 2007, PhD thesis, University of Melbourne
- Wong T., Blitz L., 2002, *ApJ*, **569**, 157
- Wong O. I., Meurer G. R., 2016, The Survey for Ultraviolet emission in Neutral Gas Galaxies (SUNGG), in preparation
- Wong O. I., et al., 2006, *MNRAS*, **371**, 1855
- Wong T., et al., 2013, *ApJ*, **777**, L4
- Yim K., van der Hulst J. M., 2015, Star formation and gas accretion in nearby galaxies, submitted to MNRAS
- Zheng Z., Meurer G. R., Heckman T. M., Thilker D. A., Zwaan M. A., 2013, *MNRAS*, **434**, 3389
- Zwaan M. A., et al., 2004, *MNRAS*, **350**, 1210